

International Journal of Vehicle Performance

ISSN online: 1745-3208 - ISSN print: 1745-3194

<https://www.inderscience.com/ijvp>

Optimisation study of aerodynamic drag based on flow field topology in box-type trucks

Zihou Yuan, Wangyang Xiang, Hongwei Zhang, Zigang Zhao

DOI: [10.1504/IJVP.2023.10058001](https://doi.org/10.1504/IJVP.2023.10058001)

Article History:

Received:	07 November 2022
Last revised:	17 May 2023
Accepted:	18 May 2023
Published online:	13 December 2023

Optimisation study of aerodynamic drag based on flow field topology in box-type trucks

Zihou Yuan

Hubei Key Laboratory of Digital Textile Equipment,
Wuhan Textile University,
Wuhan, Hubei, 430073, China

and

Key Laboratory of Concrete and Pre-Stressed Concrete
Structure of Ministry of Education,
Southeast University,
Nanjing, Jiangsu, 211189, China
Email: whuyzh@163.com

Wangyang Xiang*, Hongwei Zhang and
Zigang Zhao

Hubei Key Laboratory of Digital Textile Equipment,
Wuhan Textile University,
Wuhan, Hubei, 430073, China
Email: 2937594913@qq.com
Email: 1248708115@qq.com
Email: 2936444310@qq.com

*Corresponding author

Abstract: The research objective of this study is to solve the problem of excessive air resistance of box trucks at high speed. Taking the small box-type truck model as the object of study, the simulations were done with CFD software to simulate the external flow field of the small box-type truck driving at high speed. Under the premise of ensuring driving safety, the area at the front of the truck and the top of the carriage is identified as the area to be optimised. The local optimum criteria are used to topologise the local external flow field to be optimised, and the model is remodelled according to the optimisation results. Validation showed that a suitable optimisation scheme could be proposed by using the local optimum criteria. The design method provided in this scheme can provide a better scheme for the research of truck drag reduction, improve design efficiency and save optimisation time.

Keywords: truck; CFD simulation; local optimum criteria; flow field topology; Tosca fluid; local external flow field.

Reference to this paper should be made as follows: Yuan, Z., Xiang, W., Zhang, H. and Zhao, Z. (2024) 'Optimisation study of aerodynamic drag based on flow field topology in box-type trucks', *Int. J. Vehicle Performance*, Vol. 10, No. 1, pp.96–118.

Biographical notes: Zihou Yuan received his Master's degree at Wuhan University, September 2000–July 2002, with a research focus on structural dynamics and Doctoral degree at Wuhan University, September 2005–December 2008, with a research focus on computational fluid dynamics. His work experience is at Wuhan Textile University, July 2002–present. His research focuses on computational structural dynamics and fluid dynamics.

Wangyang Xiang studied at Wuhan University of Engineering Science from 2016 to 2020 and obtained his Bachelor's in Mechanical Design, Manufacturing, and Automation. Since 2021, he has been pursuing his Master's in Mechanical Engineering at Wuhan Textile University with a research focus on computational fluid dynamics and flow field topology.

Hongwei Zhang studied at Hubei University of Arts and Science and obtained his Bachelor's in Mechanical Design, Manufacturing, and Automation from September 2020 to June 2022. Since September 2022, he has been pursuing his Master's in Mechanical Engineering at Wuhan Textile University with a research focus on computational fluid dynamics and flow field optimisation.

Zigang Zhao studied at the College of Mechanical and Electronic Engineering, Hubei Engineering University from 2016 to 2020 and obtained his Bachelor's in Mechanical Design and Manufacturing and its Automation. Since 2021, he has been pursuing his Master's in Mechanical Engineering at Wuhan Textile University with a research focus on computational fluid dynamics and flow field optimisation.

1 Introduction

In recent years, with the transformation of consumption forms and the vigorous development of the logistics industry, box trucks have been widely used as an important means of transport. Along with the importance placed on carbon neutrality and other environmental protection issues, researchers have turned their attention to reduce the aerodynamic resistance of trucks in order to improve energy efficiency. The blunt design of the box-type trucks has a large windward area during travel, so air resistance is also extremely high. Most scholars have currently combined pneumatic and mechanical principles to design a large number of pneumatic drag reduction structures.

Harun et al. (2013) optimised the front fairing and side coverings as well as filling the gap between the truck and the container box, and then conducted model wind tunnel tests with a 1/10 scale truck model to study the effect of different aerodynamic accessories on the aerodynamic drag of heavy trucks under different operating conditions, which included a range of speeds and yaw angles, as well as different combinations. The results showed that the front fairing alone could reduce drag by around 17%. Further drag reduction up to 26% is possible using various combinations of aerodynamic fairings in different parts of the truck body. Alamaan et al. (2014) studied the effect of the tail drag reduction device on the aerodynamic drag of the trucks. It was found that an elliptical baffle with a short half-axis of 0.12m can achieve a maximum drag reduction rate of 11.1% by changing the basic geometry of the flaps. Chaitanya et al. (2014) analysed the effect of trailer shape change on aerodynamic drag and its effect on fuel consumption using the SST turbulence model, and the results of the analysis showed that the

aerodynamic drag of a diesel-powered truck was reduced by 21% and fuel consumption was reduced by 4 litres over 100 km after installing the profile modification that has been done on the basic truck-trailer model by providing a wind deflector on the truck's cabin, vortex trap, mini skirt, vortex strake, and aerodynamic revolute. Jae et al. (2017) quantitatively investigated the drag reduction effects of typical and improved cab-roof fairing (CRF) models using wind tunnel experiments and numerical simulations [coarse large eddy simulation (LES)]. The results showed that the modified (CRF) model significantly improved the flow structure and could reduce the drag by 19%. Omar et al. (2022) changed the geometry of the drag reduction device and then conducted a numerical study of drag reduction devices with different sizes and configurations using Star CCM+ software. The resistance reduction devices used in this study include steps, fins, splitters, dimples, vents backward-facing and so on. When a backward-facing step was placed at the bottom rear edge of the truck, it could reduce the drag by 9.9%. The addition of multiple round channels on both sides could reduce resistance by 6.5%, and multiple rectangular channels on both sides could reduce resistance by 5.1%. Xu and Fan (2019) designed nine types of tail drag reduction devices by combining the pneumatic drag reduction mechanism, and the pneumatic drag coefficient of the whole vehicle was reduced after installing the devices, and the maximum reduction was 7.96%. Xu et al. (2021) combined bionics to design pneumatic drag reduction devices for trucks and analysed the flow field of the optimised trucks. The aerodynamic drag coefficient of the entire truck was reduced after the installation of the device, with a maximum reduction of 7.96%. Feng and Zhang (2022) reported that based on the flap structure at the rear of the truck, a wind turbine was added to recover wind energy and convert it into drag reduction efficiency. The study found that the drag reduction effect of both flaps and fans increases and then decreases with increasing flap length, and the maximum drag reduction rate can reach 19.5%.

As can be seen from the above, most of them are designed by analysing the aerodynamic drag reduction mechanism and then designing the drag reduction device for trucks, and the optimisation scheme derived from the flow field topology is not very common. Therefore, this paper takes a small box-type truck as an example and, based on the local optimum criteria, conducts flow field topology study of the local external flow field of the truck at rapid speed. This study improves the optimisation efficiency of box trucks and provides a new method for the optimisation of aerodynamic drag reduction in box trucks.

2 CFD simulation and analysis of the original model

The optimisation method in this paper adopts the local optimum criteria, which is currently only available for simple flow field optimisation (Zhang et al., 2021). For complex flow fields, it is necessary to take local flow fields and optimise them individually.

The main structures of a box truck include the front end, compartment, chassis, mirrors, etc. We want to know which of these structures provides the greatest aerodynamic drag. Therefore, in this section, we first perform CFD simulations for small box trucks and then analyse the optimisation area based on the results of the CFD simulations.

2.1 Target vehicle model and computational mesh

SpaceClaim software was used to build a small box truck model and simplify the chassis, tires and other minor components. It measures 8.3 metres long, 2.7 metres wide and 3.23 metres high, respectively. Figure 1 shows a small box truck model.

To simulate the unconstrained free-stream conditions, a virtual rectangular wind tunnel is simulated and define the blockage ratio not exceeding 2% (Feng and Zhang, 2022) (blockage ratio: the ratio of the projected area of the model in the wind tunnel to the cross-sectional area of the wind tunnel). The outlet is set at a distance of ten times the car length from the rear of the truck, the inlet is five times the car length from the small box truck, the upper end of the computational domain is five times the height of the vehicle from the roof, and the width of the computational domain is ten times the width of the vehicle, as shown in Figure 2.

Figure 1 3D model of a small van (see online version for colours)

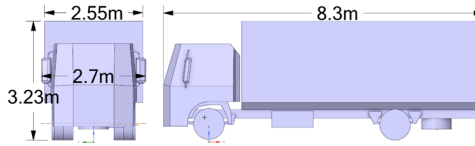
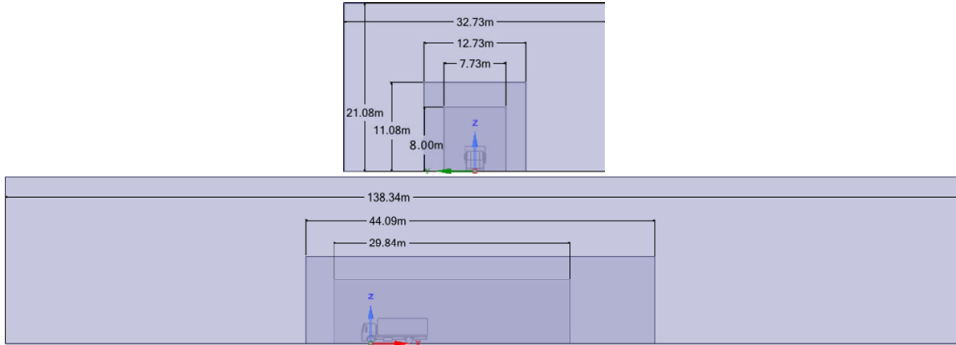


Figure 2 Computational domain (see online version for colours)



To maintain better resolution around the vehicle, hierarchical allocation is carried out with ICEM software. In order to capture the steeper gradient of the flow properties within the boundary layer, high mesh resolution is needed near the wall surface. As a result, the height of the vehicle's first layer grid must be calculated. The height of the first layer grid y is calculated as follows (Wang and Li, 2022):

$$\text{Re} = \frac{\rho U \cdot H}{\mu} \quad (1)$$

$$C_f = 0.0592 \text{Re}^{-\frac{1}{5}} \quad (2)$$

$$\tau_w = C_f \cdot \frac{1}{2} \rho U^2 \quad (3)$$

$$u^* = \sqrt{\frac{\tau_w}{\rho}} \tag{4}$$

$$y = \frac{y^+ \mu}{\rho u^*} \tag{5}$$

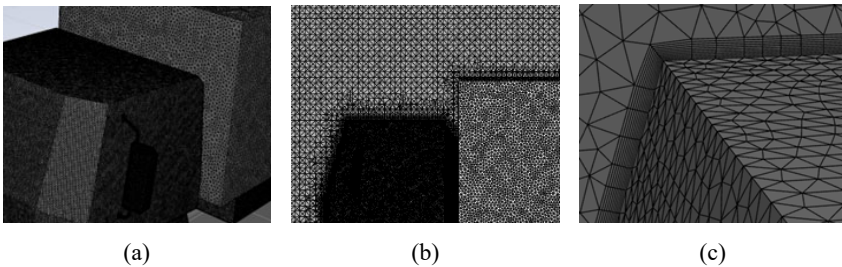
where ρ is the air density. 1.225 kg/m^3 ; U is the flow velocity. 30 m/s ; H is the characteristic length. 3.23 m and μ is the dynamic viscosity. $1.789 \times 10^{-5} \text{ kg/(m}\cdot\text{s)}$; Reynolds number is calculated from the above equation (1) (Wang and Li, 2022) $Re = 6.635 \times 10^6$; When $10^5 < Re < 10^7$ using equation (2) to calculate the wall friction coefficient C_f ; τ_w is the wall shear stress. u^* is the wall friction velocity. In this paper, y^+ is predicted to be 90. The grid height of the first layer is calculated as y is 1.18 mm .

The surface mesh is triangular, the surface mesh size of the small box truck head is 20 mm , the rearview mirror surface mesh size is 10 mm , the chassis and tire surface mesh sizes are 20 mm , and the packing case surface mesh size is 40 mm . Ten prisms were added to the front and compartments of the van with a growth ratio of 1.05 per layer. Such a grid setup meets the requirements for the boundary layer in SAE Standard J2966 (SAE International Surface Vehicle Recommended Practice, 2021). While the volume is filled with tetrahedral meshes generated, which obeys a 1.2 maximum growth rate. Encrypted regions filled with a smaller mesh size are created to capture the flow physics. Mesh sizes inside encrypted regions is varied to perform the grid independence study. Table 1 presents the mesh independence study. Because the C_d discrepancy is less than 0.6% with 1,546,663 total nodes, the same mesh topology is used throughout this study. Figure 3 shows an overview of the present computational meshes.

Table 1 Mesh independence study.

Total nodes	Drag coefficient C_d	Discrepancy
913,103	0.4688	1.76%
1,364,999	0.4727	0.95%
1,546,663	0.4772	—
1,947,726	0.4801	0.60%

Figure 3 (a) Surface mesh of the truck, rear-view mirrors, and carriage, (b) Vertical cut-plane view of the mesh volume mesh near the model and (c) Cut-plane view of boundary layer mesh



The drag coefficient C_d is defined as follows:

$$C_d = \frac{F_d}{\frac{1}{2}\rho U_\infty^2 A} \tag{6}$$

where A is the area of the windward side of the vehicle, ρ is the air density, and U_∞ is the inlet wind speed.

2.2 Boundary condition

In this study, ANSYS Fluent software was used for simulation, and the standard wall function was selected and the standard $k-\epsilon$ turbulence model was used to simulate the flow field external to the truck. The boundary settings are shown in Table 2.

Table 2 Setting of boundary conditions

Boundary of domain	Conditions
Inlet	Velocity inlet: velocity magnitude $V = 30$ m/s, turbulent intensity $I = 0.5\%$
Outlet	Pressure outlet: gauge pressure $P = 0$ Pa, turbulent intensity $I = 5\%$
Wall surface	Stationary wall, no-slip

2.3 CFD simulation results and analysis of the original flow field

Through CFD software simulation we know that the aerodynamic drag F_d on the whole vehicle is 2209.988N; the drag coefficient C_d is 0.4772. G. Wei, et al. in 2022 mentioned in the literature (Wei et al., 2022) that the aerodynamic drag on the AHV mainly comes from the following four areas:

- 1 the forebody stagnation region
- 2 the gap region between the tractor and the trailer
- 3 the under-body 2 region of the truck and the trailer
- 4 the rear end of the trailer, as shown in Figure 4.

In the literature of 2020 (Wang et al., 2020), Wang et al. analysed that the air resistance of the front end and cargo box of the truck occupies 86.98% of the whole vehicle when travelling at a speed of 100 km/h, while the air resistance of the mirrors and tires only accounts for 13.02% of the whole vehicle. Although there are differences in appearance between heavy-duty vehicles and small box trucks, it provides valuable guidance for the development of airflow control devices for small box trucks. In the present study, we can find through Figure 5, the front windward side of the truck and the top of the windward side of the box produced a large positive pressure, which is the main source of differential pressure resistance position. This phenomenon is similar to the simulation results in the literature (Wang et al., 2020). However, this paper takes into account that the addition of a drag reduction device in front of the cockpit may cause a blind spot in the driver’s field of vision, which will threaten the driving safety of the truck. Therefore, this study finally decided to optimise the area above the cockpit and above the carriage to

improve the air flow performance above the cockpit and carriage, thus reducing the aerodynamic drag of the box truck.

Figure 4 Aerodynamic drag contributing regions on an AHV (see online version for colours)

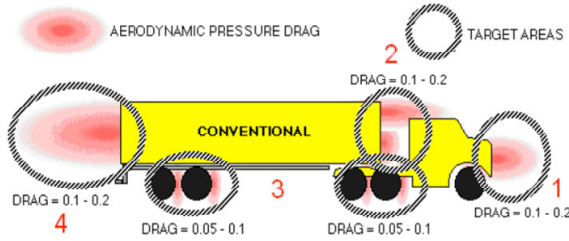
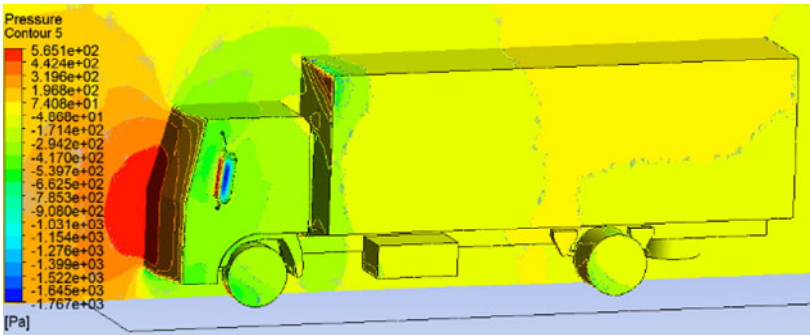


Figure 5 Contours of static pressure on the vehicle body and contours of static pressure along the symmetry plane (see online version for colours)



3 Local external flow field topology

According to the analysis in the previous section, the space to be optimised is determined. Next, it requires the flow field topology optimisation of the specified optimisation space. In this section, the theory and steps of the flow field topology optimisation employed in this study will be presented.

3.1 Optimisation method

In this study, we used a local optimum criteria to optimise the local external flow field of small box trucks, which was also called the quasi-sensitivity (QS). The QS is based on the backflow theory studied by Moos et al. (2004), where backflow, shunt and vortices are the main sources of energy loss, and the optimal nature of the QS is the generation of inhibitory backflow.

Before optimisation, the reference velocity v_{ref} is obtained by numerical simulation within the flow field with a high-viscosity fluid that does not produce backflow, and then the actual flow velocity U is obtained in the optimisation and QS is calculated by the following equation (Zhang et al., 2021).

$$QS_n = \frac{(v_{ref} \cdot U)_n}{(|v_{ref}| \cdot |U|)_n} \tag{7}$$

where n denotes the n th grid point. From equation (7), QS is the quasi-sensitivity, which represents the angular difference between the reference velocity vector and the actual velocity vector of the flow field and takes a value in the range of $[-1 \sim 1]$.

A line search algorithm was used in order to achieve the elimination of all backflow zones. It should be noted that the algorithm is not run for porosity but for the design variable γ (Iseler and Martin, 2017):

$$\gamma_k = \begin{cases} \gamma_{k-1} - \lambda QS \gamma_{k-1} & QS > 0 \\ \gamma_{k-1} - \lambda QS (1 - \gamma_{k-1}) & QS \leq 0 \end{cases} \tag{8}$$

With $\gamma \in \{0, \dots, 1\}$ in iteration k , λ denotes the step size. Based on the design variable γ , $\alpha(\gamma)$ can then be calculated (Xian-Bao et al., 2015):

$$\alpha(\gamma) = \alpha_{min} + (\alpha_{max} - \alpha_{min}) \frac{m(1-\gamma)}{m+\gamma} \tag{9}$$

where m is a real and positive parameter used to tune the shape of $\alpha(\gamma)$. The variable α is the Brinkman penalisation coefficient ($\alpha > 0$) (Othmer, 2008).

In order to take into account the design variable γ of the medium, the governing equations in the topology optimisation problem are defined. The momentum balance equation is expressed considering the resistance imposed by the medium on the flow. This resistance is introduced into the Navier-Stokes equations for steady-state flow through the Brinkman term αv , which defines the governing equations in fluid topology problems as follows (Pietropaoli et al., 2017).

$$\nabla \cdot \bar{v} = 0 \tag{10}$$

$$(\bar{v} \cdot \nabla) \bar{v} = -\nabla p + \nabla (2\mu D(\bar{v})) - \alpha \bar{v} \tag{11}$$

where v , p , μ , and D denote the velocity vector, pressure, effective kinematic viscosity, and rate of strain tensor, respectively.

From equations (10) and (11) above, it can be seen that equation (11) simplifies to the Navier-Stokes equation when $\alpha = 0$. As α increases, the velocity v decreases. When α is large enough, the magnitude of the velocity v is uniformly close to 0, simulating solid matter.

To better understand this optimisation method, this paper explains the theory with a simple geometry. The essence of the flow field topology based on the local optimum criteria is to turn the backflow region in the specified space into a solid, so as to reduce the backflow. Iseler and Martin (2017) explained this process in 2017, and this paper further built on it.

Figure 6 Available design space geometry (see online version for colours)



The available design space geometry shown in Figure 6 is a circular pipe with a necking in the front half of this pipe with a radius smaller than the pipe body, with the flow inlet on the left and the flow outlet on the right.

Figure 7 Velocity vectors inside of initial geometry (see online version for colours)

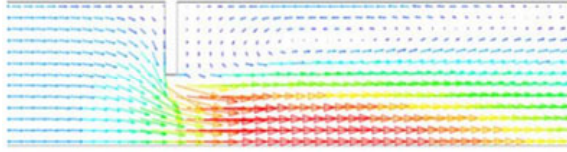


Figure 7 shows the velocity vectors inside the initial geometry structure inside this circular pipe. It is easy to see in this velocity vectors that there are distinct backflow regions in the front and back ends of the incident. Iseler J. and Martin T.J. used the local optimal criteria to find these return regions and reduced the velocity of the fluid in the return regions.

Figure 8 Flow field after optimisation run (see online version for colours)

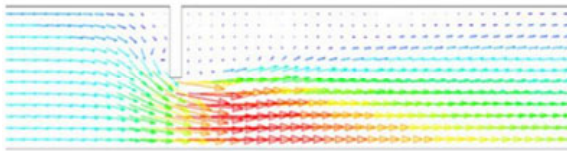


Figure 8 shows the flow field after optimisation run of this circular pipeline. It is obvious from Figure 8 that when optimised for operation, in backflow zones, the velocity of the fluid slows down to close to 0 by using equation (11), and the fluid is converted from a flowing state to a solidification-like state. However, in zones without backflow, the velocity and direction of the fluid remain predominantly unchanged.

Figure 9 Optimisation result (see online version for colours)



Figure 9 shows the optimisation result of this pipe, where the red part is the solid and the blue part is the fluid. The zone corresponding to the solid is exactly the zone where the fluid velocity is close to 0 in Figure 8. With careful observation, we can find that the solid wall is not smooth, thus the solid surface needs to be smoothed.

Figure 10 Design proposal after extraction and smoothing (see online version for colours)

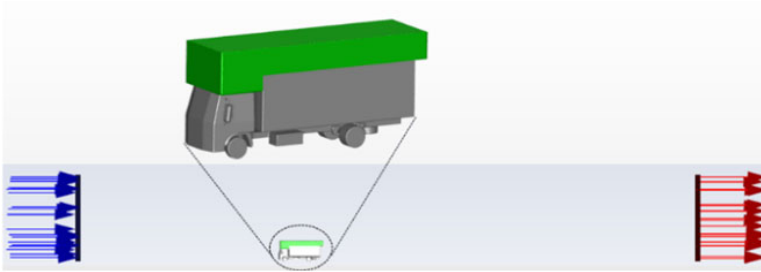


Figure 10 shows the design proposal after extraction and smoothing. Since the whole design is based on the magnitude of the backflow to control the solid shape, it is necessary to verify whether the design solution can meet the final design requirements after the design results are obtained.

3.2 Setting of the local outflow field to be optimised

Based on the results of the analysis in Section 2.4, the flow field area at the top of the headstock and the top of the carriage is then designated as the local external flow field to be optimised, namely the green area in Figure 11. In order to provide realistic flow directions around the local external flow field to be optimised, the same virtual wind tunnel as in Section 2.2 was built outside the local external flow field to be optimised in this study. In Figure 11, blue arrows are the inlet boundary and red arrows are the outlet boundary. As with chapter Section 2.2, the computational domain and meshing operations are repeated with ICEM.

Figure 11 Develop optimised flow field (see online version for colours)

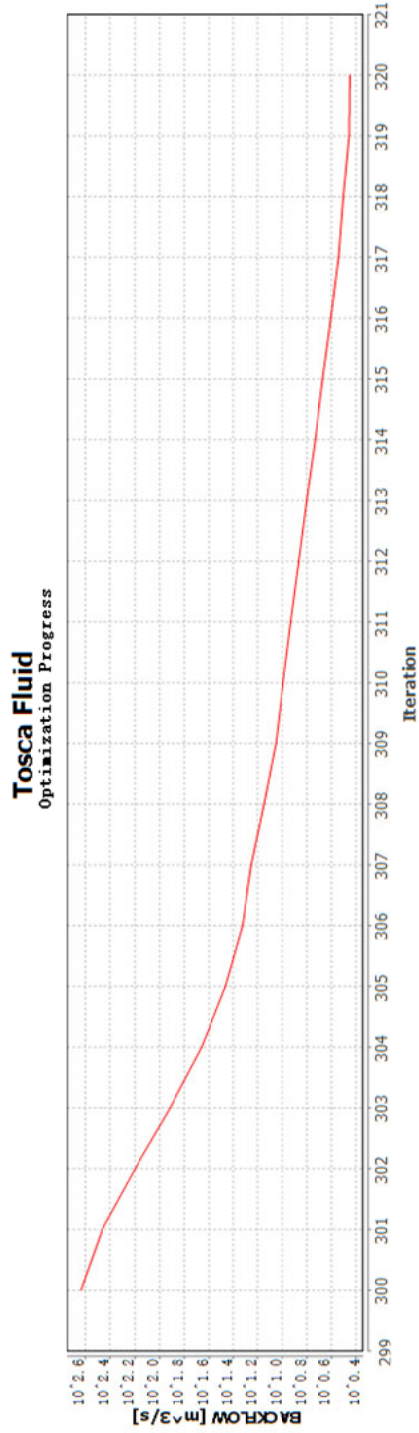


3.3 Solver settings and flow field optimisation settings

The mesh files from Section 3.3 were imported into the ANSYS Fluent module and the same boundary layer setup as in Section 2.2 was repeated and exported the *cas* file after the initialisation. Open the previous *cas* file in Tosca fluid. The topology flow based on Tosca fluid software was as follows:

- 1 The definitions of outlet and inlet were repeated in the Tosca fluid software so that the boundary layers were consistent with those in ANSYS Fluent.
- 2 The optimised flow field was specified. Set the green area in Figure 11 as the optimised area.
- 3 The objective optimisation and the number of iterations were set in Tosca fluid software. The convergence of fluid optimisation can be defined as a state where the backflow tends to a plateau and a minimum, indicating that the optimisation process has converged.
- 4 After the Tosca fluid software started the optimisation, we opened the *cas* file to run the ANSYS Fluent solver. After the completion of the iteration, the backflow monitoring curve is shown in Figure 12.
- 5 Post-process and export optimisation results.

Figure 12 Tosca fluid iterative curve (see online version for colours)



The flow chart of flow field topology optimisation is shown in Figure 13, and the optimisation results are shown in Figure 14.

Figure 13 Flow chart of flow field topology optimisation

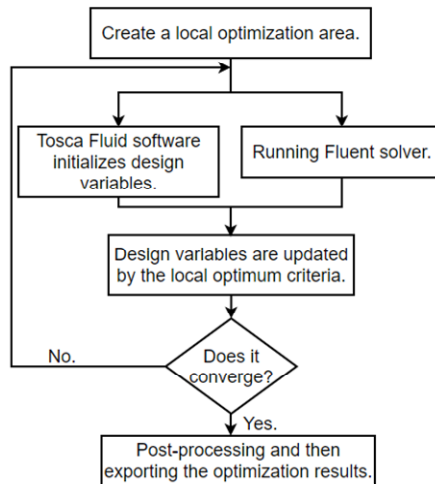
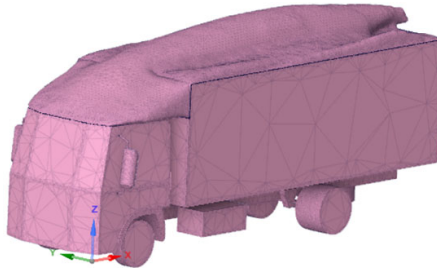


Figure 14 Optimisation results (see online version for colours)



It is essential to emphasise here that the optimisation results shown in Figure 14 are determined by how much backflow is present in the external flow field to be optimised. As can be seen from the Tosca fluid iteration curve shown in Figure 12, this iteration curve is monitoring the backflow, and the optimisation results in Figure 14 are obtained when the backflow stabilises and reaches a minimum value. In other words, the optimisation results in Figure 14 can only indicate that the geometry can further reduce the backflow. However, this optimisation result is not yet able to determine whether the requirement of aerodynamic drag reduction of box truck is achieved, so this paper needs to perform CFD simulation on the optimisation result and then make an analysis.

4 Analysis of flow field optimisation results

In this paper, the optimisation results of the box truck model in the Section 4.4 were obtained by controlling the return flow. Since the reduction in backflow is not directly expressed as a reduction in aerodynamic drag, the purpose of this section is to perform an aerodynamic drag analysis of the optimisation results.

Based on the optimisation results for the local external flow field, the truck model was reconstructed and the CFD simulation described above was repeated. Table 3 compares the aerodynamic drag and aerodynamic drag coefficient of the small box truck before and after optimisation. As can be seen from Table 1, when the truck is optimised, the aerodynamic drag is 1,816.289N and the aerodynamic drag coefficient is 0.3251. Although the projected area on the windward face of the optimised small box truck has increases from 8.4 m² to 10.1 m², the aerodynamic drag has been reduced, and the air resistance has been reduced by 324.851N, with the drag reduction rate reaching 29.66% relative to the original small box truck.

Table 3 Comparison of aerodynamic drag and aerodynamic drag factor before and after optimisation

	<i>Original model</i>	<i>The optimised model</i>	<i>Drag reduction ΔF_d/drag reduction ratio ΔD</i>
Aerodynamic drag F_d	2,209.988N	1,816.289N	393.699N
Aerodynamic drag coefficient C_d	0.4772	0.3251	31.87%

Where the amount of drag reduction ΔF and the drag reduction rate ΔD are defined by the following equations:

$$\Delta F_d = F_{d0} - F_{d1} \tag{12}$$

$$\Delta D = \frac{C_{d0} - C_{d1}}{C_{d0}} \tag{13}$$

where F_{d0} is the aerodynamic drag of the original model, F_{d1} is the aerodynamic drag of the optimised model, C_{d0} is the aerodynamic drag coefficient of the original model, and C_{d1} is the aerodynamic drag coefficient of the optimised model.

Figure 15 Contours of static pressure on the vehicle body after optimisation and contours of static pressure along the symmetry plane after optimisation (see online version for colours)

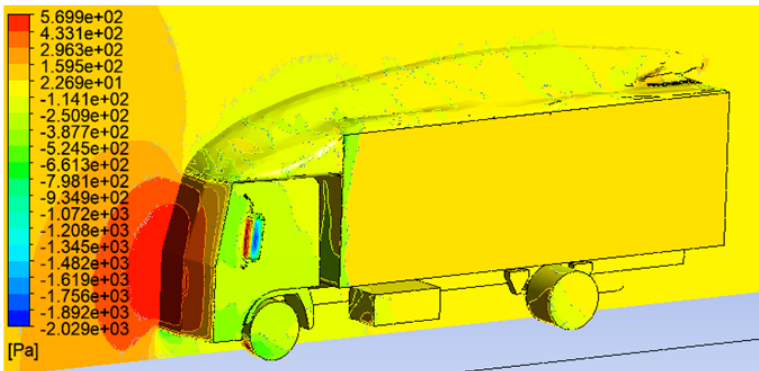


Figure 16 Five observation planes (see online version for colours)

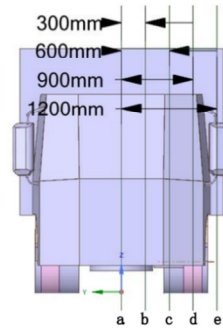


Figure 17 Velocity vectors for different observation planes of the truck (see online version for colours)

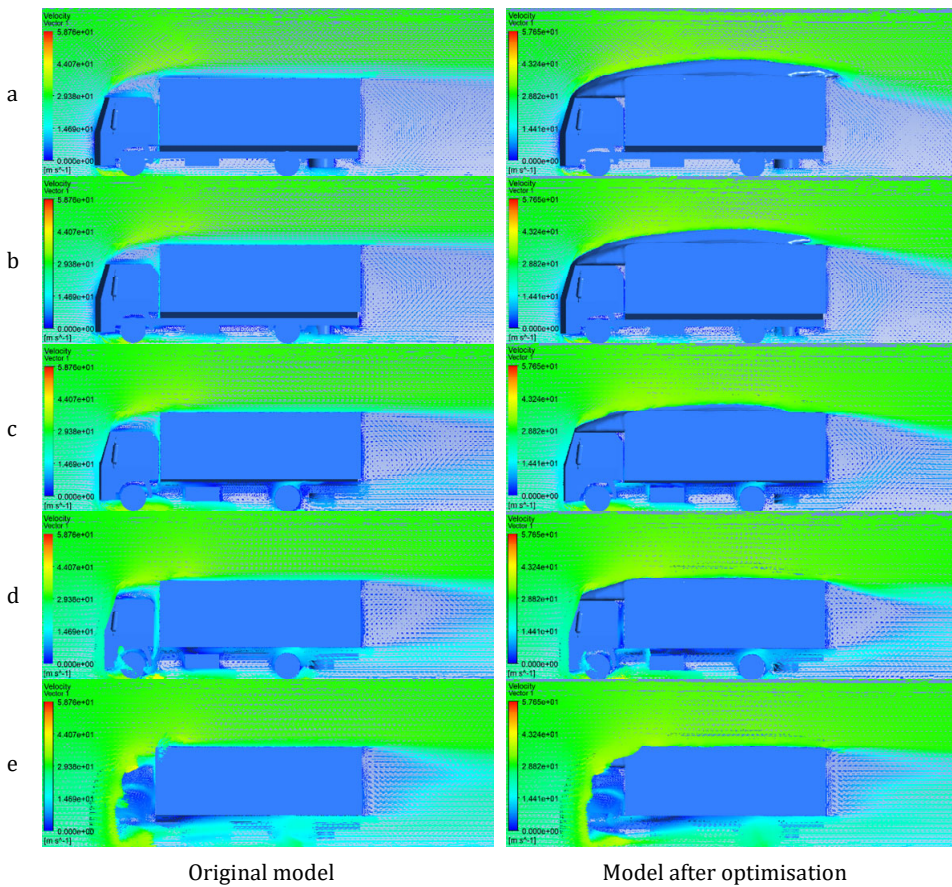


Figure 15 shows the contours of static pressure on the vehicle body after optimisation and the contours of static pressure along the symmetry plane after optimisation. In comparison to Figure 5, the area of high pressure between the top of the front end and the

compartment of the optimised small box truck has vanished, and the positive pressure in the windward face has significantly decreased.

In order to show the external flow field of the small box truck more comprehensively, we intercepted four observation planes (a)(b)(c)(d). Observation plane (a) is the symmetry plane of small box truck, observation plane (b) is 300 mm away from observation plane (a), observation plane (c) is 600 mm away from observation plane (a), observation plane (d) is 900 mm away from observation plane (a), and observation plane (e) is 900 mm away from observation plane (a), as shown in Figure 16.

Figure 17 compares the different observation plane velocity vectors of the small box truck before and after the optimisation. Combined with the optimisation principle of the local optimum criterion in Section 4, it is easy to see that the region of poor flow performance in the local external flow field to be optimised has been replaced by a solid, and the shape of the solid also has excellent aerodynamic drag reduction properties.

Figure 18 Velocity streamlines for different observation planes of the truck (see online version for colours)

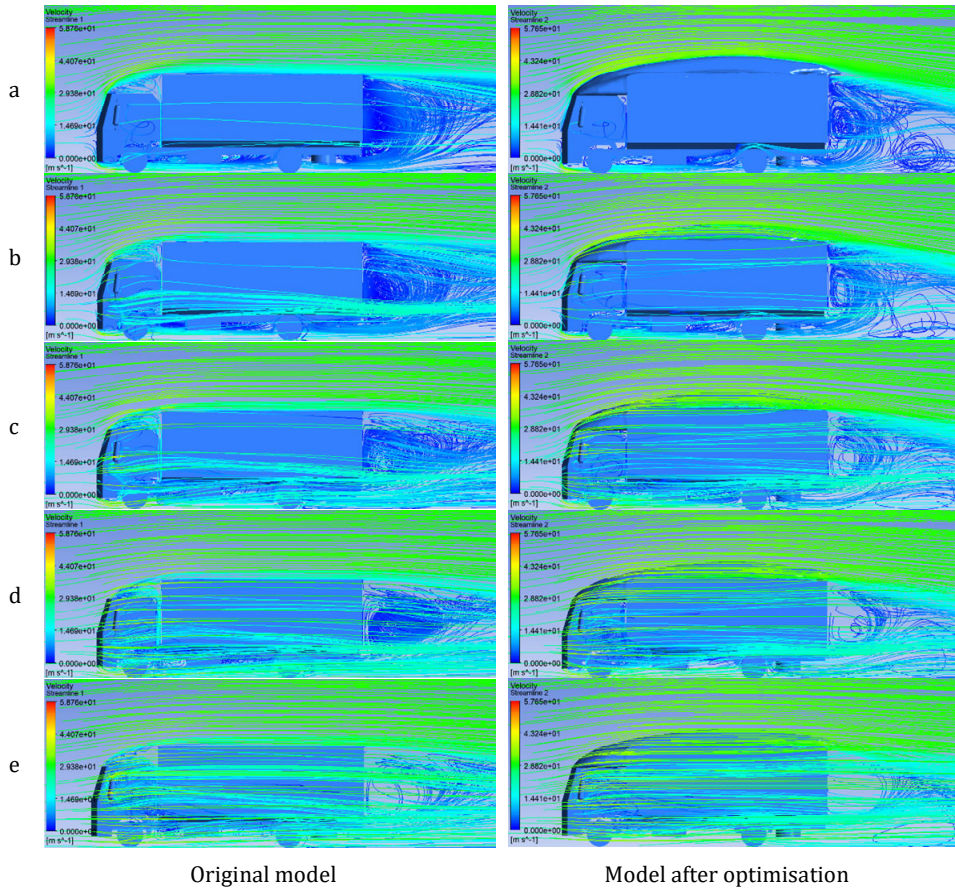
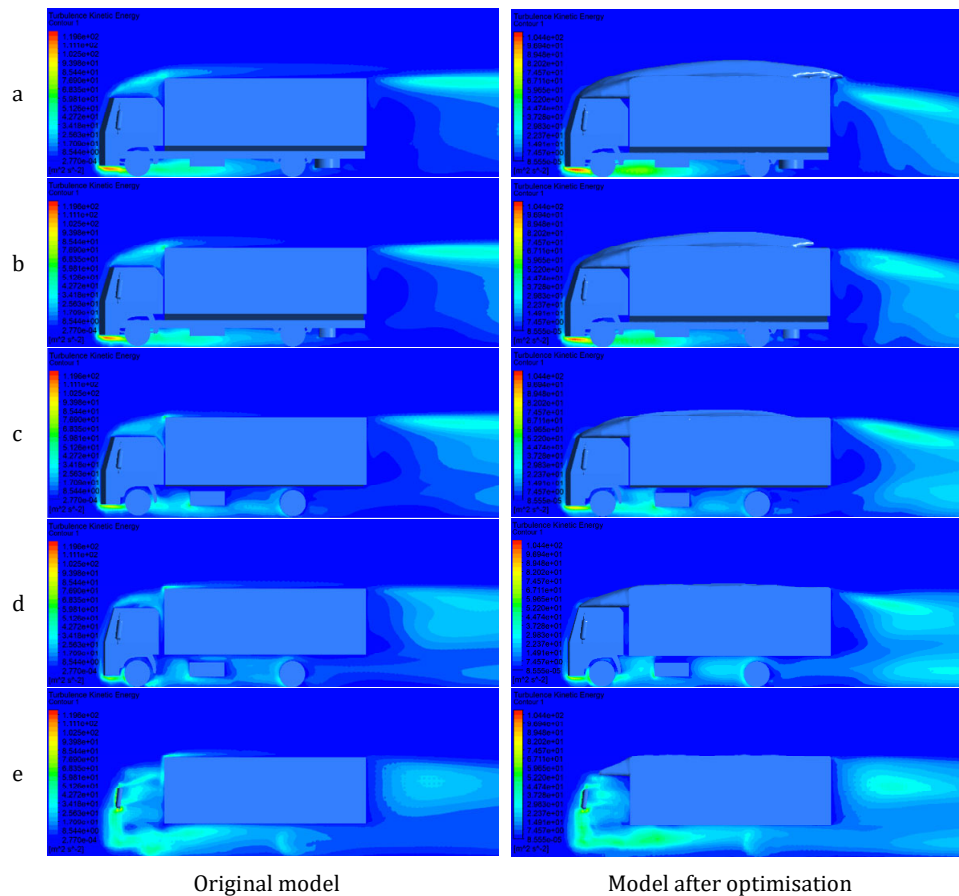


Figure 18 compares the different observation plane velocity streamline of the small box truck before and after optimisation. As can be seen from Figure 18, the optimised airflow velocity at the top of the front end and the top of the compartment is significantly accelerated, and the wake vortex generated at the rear of the truck is also reduced. It is shown that this optimisation not only has significantly improved the drag reduction in the specified optimised area, but also has improved the performance of the flow field at the rear of the truck.

Figure 19 compares the cloud diagram of turbulent kinetic energy of the different observation plane before and after the optimisation of the small box truck. According to the law of conservation of energy, the turbulent kinetic energy can be used to represent the amount of energy dissipated around the car. The greater the turbulent kinetic energy, the greater the energy loss, which represents greater aerodynamic drag. As can be seen from Figure 19, the optimised turbulent kinetic energy is significantly reduced at the top of the front end and above the carriage, as well as the turbulent kinetic energy at the rear of the carriage is also reduced.

Figure 19 Turbulent kinetic energy distribution for different observation plane of van model (see online version for colours)



Original model

Model after optimisation

From this summary, the optimised small box-type truck has an obvious effect of drag reduction, which verifies the feasibility and correctness of this optimisation method applied in the external flow field of the truck.

5 Verification of advanced results of flow field topology optimisation

In order to verify whether the local optimisation criterion can obtain a better drag reduction scheme than the traditional optimisation, (i.e., optimisation based on the aerodynamic drag reduction mechanism), this paper combines the aerodynamic drag reduction mechanism and designs five groups of drag reduction devices as a control.

The control group is provided by providing a wind deflector in the cab of the truck and covering the top of the carriage with curved panels as shown in Figure 20. The idea of adding a deflector at the front of the car is derived from the current mainstream drag reduction scheme. The idea of covering the top of the carriage with curved panels originated from the optimised design of bionic drag reduction proposed by Xu et al. (2021), which is similar to the abdominal shape of fish and dolphins. In order to obtain the best curved height at the top of the carriage, five combinations of devices with a curved height H of 350 mm, 300 mm, 250 mm, 200 mm and 150 mm were designed for comparison.

Figure 20 Schematic diagram of control model (see online version for colours)

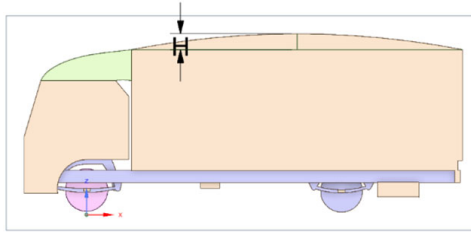
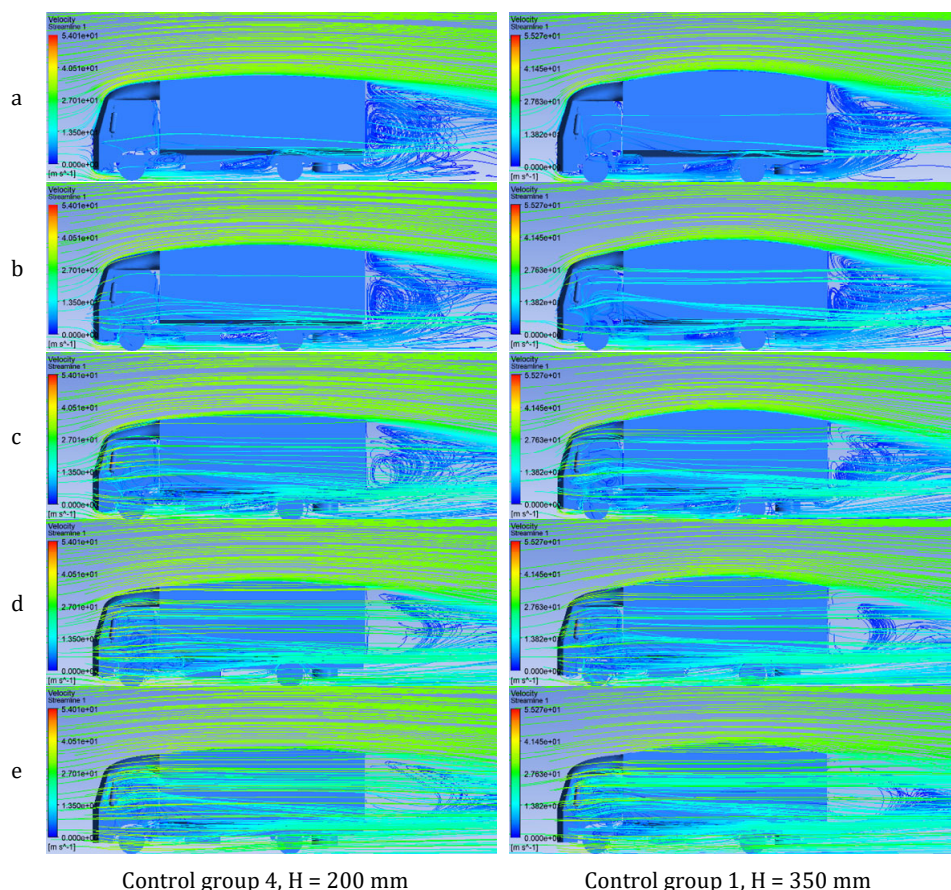


Table 4 Comparison of drag reduction effect in control group

<i>Model</i>	<i>Area on the windward face A</i>	<i>Aerodynamic drag F_d</i>	<i>Drag reduction ΔF_d</i>	<i>Aerodynamic drag coefficient C_d</i>	<i>Drag reduction ratio ΔD</i>
Control group 1, $H = 350$ mm	9.4 m ²	1,847.342N	362.646N	0.3581	24.97%
Control group 2, $H = 300$ mm	9.2 m ²	1,846.821N	363.167N	0.3633	23.88%
Control group 3, $H = 250$ mm	9.1 m ²	1,885.145N	324.843N	0.3764	21.13%
Control group 4, $H = 200$ mm	8.9 m ²	1,823.412N	386.576N	0.3697	22.54%
Control group 5, $H = 150$ mm	8.8 m ²	1,827.312N	382.676N	0.3761	21.19%

Table 4 compares the aerodynamic drag, drag reduction, aerodynamic drag coefficient and drag reduction rate of these five control groups. As can be seen from Table 4, the five drag reduction devices designed by combining aerodynamic drag reduction mechanisms all effectively reduced the aerodynamic drag and aerodynamic drag coefficient of the small box trucks, reaching a maximum drag reduction of 386.576N (control group 4) and a maximum drag reduction rate of 24.97% (control group 1). However, none of them exceed the drag reduction rate of 324.851N and the drag reduction rate of 31.87% achieved by the flow field topology optimisation. Figure 21 shows the velocity trajectories for control group 4 and control group 1 for different observing planes. Compared with the model with optimised flow field topology, the airflow above the control model is slower, and it can be noticed from the observation plane (c) that there is a clear section of deceleration region when the airflow passes above the van. Figure 22 shows the turbulent kinetic energy clouds for different observation surfaces of control group 4 and control group 1, from which we can find that the turbulent kinetic energy above the head of the vehicle is still larger. Therefore, we use the optimisation methods that can provide better aerodynamic drag reduction effect for box trucks.

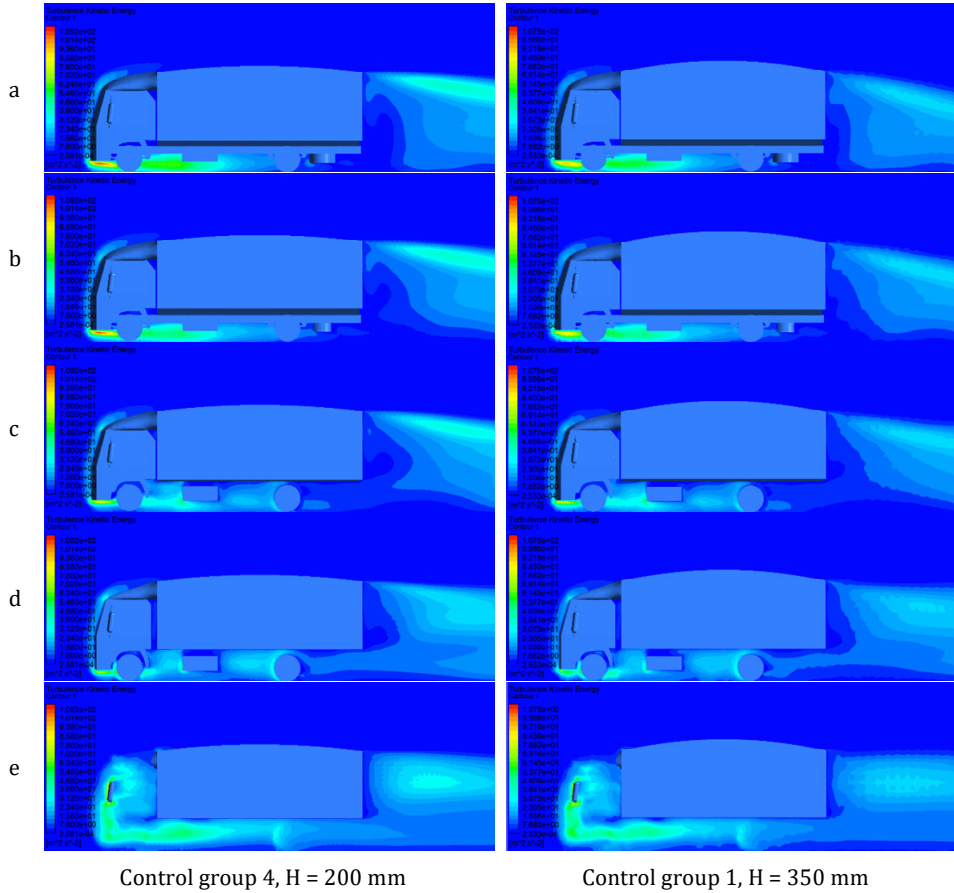
Figure 21 Velocity streamlines for different observation surfaces of control group models (see online version for colours)



Control group 4, H = 200 mm

Control group 1, H = 350 mm

Figure 22 Turbulent kinetic energy for different observation planes of control group models (see online version for colours)



6 Verification of drag reduction effect when using different turbulence models

As the turbulence model used in this experiment is the standard $k-\epsilon$ model, Table 5 compares the drag reduction effect of the original and optimised models and the five control groups when using different turbulence models to verify whether this optimisation result also has excellent drag reduction effect with different turbulence models. Additionally, to better compare the differences between different turbulence models, Figure 23 and Figure 24 respectively illustrate the drag and drag coefficient of the vehicle when using four turbulence models. Based on these data, it can be observed that while there is a slight difference in the drag reduction effect of the vehicle when using different turbulence models, the optimised model obtained in this study still achieves the best drag reduction effect.

Table 5 Comparison of drag reduction effect when using different turbulence models

<i>Turbulence model</i>	<i>Truck model</i>	<i>Aerodynamic drag F_d</i>	<i>Drag reduction ΔF_d</i>	<i>Aerodynamic drag coefficient C_d</i>	<i>Drag reduction ratio ΔD</i>
Realisable $k-\epsilon$	Original model	2,166.209N	/	0.4675	/
Realisable $k-\epsilon$	The optimised model	1,711.767N	454.442N	0.3064	34.46%
Realisable $k-\epsilon$	Control group 1, H = 350 mm	1,766.849N	399.360N	0.3425	26.74%
Realisable $k-\epsilon$	Control group 2, H = 300 mm	1,749.895N	416.314N	0.3442	26.37%
Realisable $k-\epsilon$	Control group 3, H = 250 mm	1,844.414N	321.795N	0.3682	21.24%
Realisable $k-\epsilon$	Control group 4, H = 200 mm	1,731.339N	434.870N	0.3551	24.91%
Realisable $k-\epsilon$	Control group 5, H = 150 mm	1,773.478N	392.731N	0.3650	21.92%
Standard $k-\omega$	Original model	1988.008N	/	0.4291	/
Standard $k-\omega$	The optimised model	1,760.540N	227.468N	0.3151	26.57%
Standard $k-\omega$	Control group 1, H = 350 mm	1,785.476N	202.532N	0.3461	19.34%
Standard $k-\omega$	Control group 2, H = 300 mm	1,840.334N	147.674N	0.3620	15.64%
Standard $k-\omega$	Control group 3, H = 250 mm	1,965.639N	22.369N	0.3924	8.55%
Standard $k-\omega$	Control group 4, H = 200 mm	1,775.604N	212.404N	0.3601	16.08%
Standard $k-\omega$	Control group 5, H = 150 mm	1,778.640N	209.368N	0.3661	15.15%
SST $k-\omega$	Original model	2,021.840N	/	0.4364	/
SST $k-\omega$	The optimised model	1,737.767N	284.073N	0.3110	28.73%
SST $k-\omega$	Control group 1, H = 350 mm	1,794.568N	227.272N	0.3478	20.30%
SST $k-\omega$	Control group 2, H = 300 mm	1,808.044N	213.796N	0.3557	18.49%
SST $k-\omega$	Control group 3, H = 250 mm	1,913.302N	108.538N	0.3820	12.47%
SST $k-\omega$	Control group 4, H = 200 mm	1,741.633N	280.207N	0.3531	19.09%
SST $k-\omega$	Control group 5, H = 150 mm	1,740.132N	281.708N	0.3581	17.93%

Figure 23 The aerodynamic drag of the vehicle under different turbulence models (see online version for colours)

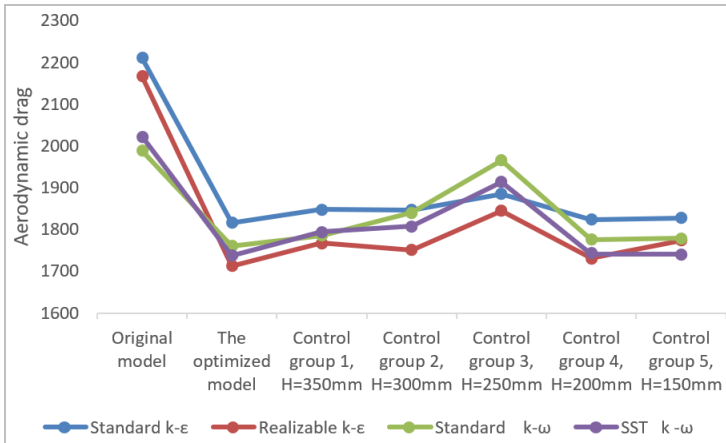
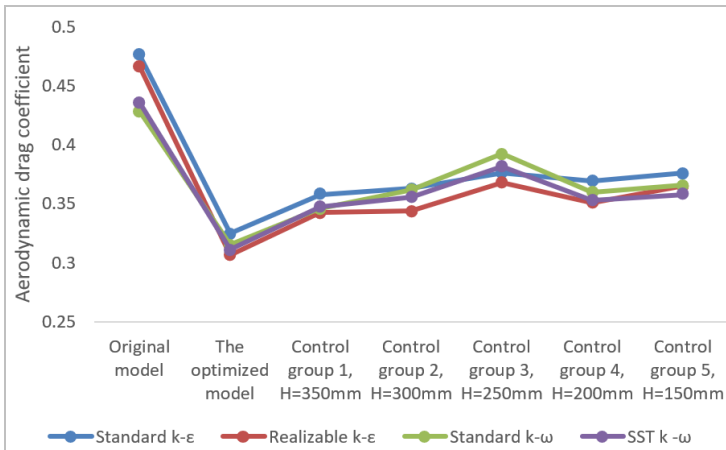


Figure 24 The aerodynamic drag coefficient of the vehicle under different turbulence models (see online version for colours)



7 Conclusions

The simulation analysis of a small box truck in an air flow field with a head-on wind speed of 30 m/s was carried out by the ANSYS Workbench simulation platform and the flow field topology of the local external flow field of the small box truck in Tosca fluid using the ANSYS Fluent solver, and the following conclusions were obtained.

- 1 The local optimal criteria in the Tosca fluid software were used to optimise the local external flow field of a small box truck. The analytical results show that the optimisation scheme provided by this method effectively reduces the generation of backflow in the specified space, significantly improves the fluid performance of the small box truck, and reduces the air resistance of the truck.

- 2 In contrast to the drag reduction devices designed according to the pneumatic drag reduction mechanism, the local external flow field topology optimisation method proposed in this study provides a better drag reduction scheme and saves time for optimal design without involving structural parametric modelling for small box-type trucks. It is shown that the optimisation scheme provided by this method effectively reduces the backflow generation in the specified space, significantly improving the fluid performance of the small box truck and reducing the air resistance of the truck.

At the same time, there are many problems in this study that need to be improved, for example, there is currently only one state of motion, lack of research on multiple velocities, lack of research on multiple yaw angles, lack of research on combining flow field topology optimisation with traditional optimisation, and lack of research on manufacturing real objects for verification, which will also be the content of our future research. Finally, as authors, we hope to make progress together with researchers all over the world, so that technology can improve our living environment and make the world a better place.

References

- Alamaan, A. et al. (2014) 'Passive drag reduction of square back road vehicles', *Journal of Wind Engineering and Industrial Aerodynamics*, Vol. 134, pp.30–43.
- Chaitanya, C. et al. (2014) 'Analyzing the profile modification of truck-trailer to prune the aerodynamic drag and its repercussion on fuel consumption', in *Conference Analyzing the Profile Modification of Truck-trailer to Prune the Aerodynamic Drag and its Repercussion on fuel Consumption*, pp.1208–1219.
- Feng, Y. and Zhang, H. (2022) 'Study on aerodynamic drag reduction device based on rear wind energy harvesting', *Acta Aeronautica et Astronautica Sinica*, Vol. 43, No. S2, pp.183–194 [online] <https://kns.cnki.net/kcms/detail/11.1929.V.20220817.1520.026.html> (access 2022).
- Harun, C. et al. (2013) 'A study on aerodynamic drag of a semi-trailer truck' in a *Conference Study on Aerodynamic Drag of a Semi-trailer Truck*, pp.201–205.
- Iseler, J. and Martin, T.J. (2017) 'Flow topology optimization of a cooling passage for a high pressure turbine blade', *ASME Turbo Expo 2017: Turbomachinery Technical Conference and Exposition, GT 2017*, 26–30 June, American Society of Mechanical Engineers (ASME), International Gas Turbine Institute, Charlotte, NC, USA.
- Jae, K.J. et al. (2017) 'Salient drag reduction of a heavy vehicle using modified cab-roof fairings', *Journal of Wind Engineering and Industrial Aerodynamics*, Vol. 164, pp.138–151.
- Jeffrey, L. and Shih-Hsiung, C. (2022) 'Aerodynamic of a refrigerated truck and improvement to reduce its aerodynamic drag', <http://dx.doi.org/10.1177/09544070221113128> (accepted 16 June 2022).
- Moos, O. et al. (2004) *Bionic Optimization of Air-Guiding Systems*, SAE Technical Papers [online] <https://www.scopus.com/inward/record.uri?partnerID=HzOxMe3b&scp=79959831088&origin=inward> (accessed March 2004).
- Omar, A.A. et al. (2022) 'Passive drag reduction of the square back truck body', *International Journal of Automotive and Mechanical Engineering*, Vol. 19, No. 3, pp.9892–9908.
- Othmer, C (2008) 'A continuous adjoint formulation for the computation of topological and surface sensitivities of ducted flows', *International Journal for Numerical Methods in Fluids*, Vol. 58, No. 8, pp.861–877, Wiley [online] <https://onlinelibrary.wiley.com/doi/abs/10.1002/fld.1770> (accessed March 2008).
- Pietropaoli, M. et al. (2017) 'Design for additive manufacturing: internal channel optimization', *Journal of Engineering for Gas Turbines and Power*, Vol. 139, No. 10.

- SAE International Surface Vehicle Recommended Practice (2021) *Guidelines for Aerodynamic Assessment of Medium and Heavy Commercial Ground Vehicles Using Computational Fluid Dynamics*, SAE Standard J2966.
- Wang, Q. (2022) *Analysis and Structural Optimization Offflow and Adhesion Characteristics Inmicroreactor*, Master, Qingdao University of Science & Technology (in Chinese).
- Wang, Q. et al. (2020) 'Study on aerodynamic drag reduction of a heavy truck based on aerodynamic accessories', *Automotive Engineering*, Vol. 42 No. 6, pp.746–752 (in Chinese).
- Wang, Y. and Li, P. (2022) 'The aerothermal prediction of a scramjet-propelled hypersonic vehicle based on NACA0012 airfoil', *Journal of Langfang Normal University (Natural Science Edition)*, Vol. 22, No. 3, pp.42–47 (in Chinese).
- Wei, G. et al. (2022) 'A comparative study of tail air-deflector designs on aerodynamic drag reduction of medium-duty trucks', *International Journal of Vehicle Performance*, Vol. 8, Nos. 2–3, pp.316–333.
- Xian-Bao, D. et al. (2015) 'Adaptive mesh method for topology optimization of fluid flow', *Applied Mathematics Letters*, Vol. 44, pp.40–44, Elsevier [online] <https://www.sciencedirect.com/science/article/pii/S0893965915000026> (accessed January 2015).
- Xu, J. and Fan, J. (2019) 'Effect of the rearbased drag-reducing device on the flow field at the rear of the truck', *Journal of Machine Design*, Vol. 36, No. 11, pp.56–64, in Chinese.
- Xu, J. et al. (2021) 'Optimized design of bionic pneumatic drag reduction device for heavy trucks', *Chinese Journal of Applied Mechanics*, Vol. 38, No. 3, pp.924–933, in Chinese.
- Zhang, M. et al. (2021) 'Fluid topology optimization method and its application in turbomachinery', *Journal of Propulsion Technology*, Vol. 42, No. 11, pp.2401–2416, (in Chinese) [online] <https://kns.cnki.net/kcms/detail/11.1813.V.20201229.1435.001.html> (accessed November 2021).